



**HAL**  
open science

# Numerical and Experimental Study of Wave Propagation in Water-Saturated Granular Media Using Effective Method Theories and a Full-Wave Numerical Simulation

Katsunori Mizuno, Paul Cristini, Dimitri Komatitsch, Yann Capdeville

► **To cite this version:**

Katsunori Mizuno, Paul Cristini, Dimitri Komatitsch, Yann Capdeville. Numerical and Experimental Study of Wave Propagation in Water-Saturated Granular Media Using Effective Method Theories and a Full-Wave Numerical Simulation. *IEEE Journal of Oceanic Engineering*, 2020, 45 (3), pp.772 - 785. 10.1109/JOE.2020.2983865 . hal-02871575

**HAL Id: hal-02871575**

**<https://hal.science/hal-02871575v1>**

Submitted on 17 Jun 2020

**HAL** is a multi-disciplinary open access archive for the deposit and dissemination of scientific research documents, whether they are published or not. The documents may come from teaching and research institutions in France or abroad, or from public or private research centers.

L'archive ouverte pluridisciplinaire **HAL**, est destinée au dépôt et à la diffusion de documents scientifiques de niveau recherche, publiés ou non, émanant des établissements d'enseignement et de recherche français ou étrangers, des laboratoires publics ou privés.

# Numerical and Experimental Study of Wave Propagation in Water-Saturated Granular Media Using Effective Method Theories and a Full-Wave Numerical Simulation

Katsunori Mizuno , Paul Cristini, *Member, IEEE*, Dimitri Komatitsch, and Yann Capdeville

**Abstract**—In this article, the detection of an object buried in marine sediments is investigated. Using the results from a series of experiments realized in a tank filled with water and calibrated glass beads, we evaluate the performances for a wide range of the value of the ratio  $kd$  of the grain size to the wavelength ( $k$  is the wave number and  $d$  is the grain diameter) of three types of prediction tools. The first two prediction tools are based on the definition of an equivalent model. The first tool is based on the well-known Biot–Stoll theory (BM model) while the second tool uses nonperiodic homogenization to define effective velocity and anisotropy maps representing the medium (HM model). The last prediction tool implements a time-domain full-wave numerical method, which takes into account each grain separately (GM model). It is shown that a good agreement between experiments and numerical simulations can be achieved using the BM model for the low  $kd$  regime and the HM model for high  $kd$  regime.

**Index Terms**—Biot–Stoll model, nonperiodic homogenization, time-domain full-wave numerical method, water-saturated granular media.

## I. INTRODUCTION

**A**COUSTIC systems with various operating frequencies are commonly used for the detection of objects buried in

Manuscript received May 9, 2019; revised December 27, 2019 and March 17, 2020; accepted March 20, 2020. This work was supported in part by Grant-in-Aid for Young Scientists A (17H04974) from the Japan Society for the Promotion of Science and in part by the International Training Project for Young Researchers from The University of Tokyo. This work was granted access to the French HPC resources of TGCC under allocation gen7165, mam0305, and gen0305 and of CINES under allocation A0020407165, A0030410305, and A0070410305, made by GENCI. This work was also granted access to the HPC resources of Aix-Marseille Université financed by the project Equip@Meso (ANR-10-EQPX-29-01) of the program “Investissements d’Avenir” supervised by the Agence Nationale de la Recherche under allocations b025. The work of Yann Capdeville was supported by the ANR HIWAI Grant ANR-16-CE31-0022-01. (Corresponding author: Katsunori Mizuno.)

**Associate Editor:** N. Chotiros.

Katsunori Mizuno is with the Graduate School of Frontier Sciences, The University of Tokyo, Kashiwa 277-8563, Japan (e-mail: kmizuno@edu.k.u-tokyo.ac.jp).

Paul Cristini is with the Aix Marseille Univ, CNRS, Centrale Marseille, LMA, 13013 Marseille, France (e-mail: cristini@lma.cnrs-mrs.fr).

Dimitri Komatitsch, deceased, was with the Aix Marseille Univ, CNRS, Centrale Marseille, LMA, 13013 Marseille, France.

Yann Capdeville is with the Laboratoire de Planétologie et Géodynamique, UMR6112, Université de Nantes, Centre National de la Recherche Scientifique, 44000, Nantes, France (e-mail: yann.capdeville@univ-nantes.fr).

Digital Object Identifier 10.1109/JOE.2020.2983865

marine sediments. For example, submarine pipelines with outer diameters of 0.2–1.8 m were investigated using a continuous-wave pulse subbottom profiler, which operates at 3.5 kHz [1]. Buried wooden shipwrecks under the seabed can be visualized using chirp signals with 1.5–13-kHz swept pulses [2]. Nonlinear acoustic systems, such as parametric subbottom profilers, which operate at a 50 kHz primary frequency and a 5-kHz secondary one, have been developed and used for the survey of buried deep-sea resources [3], [4]. Recently, relatively high-frequency signals of 100 kHz have been used for the precise survey of buried roots of a plant with outer diameters of 5–10 cm [5]. Even higher frequency signals with a center frequency of 1 MHz are just beginning to be used for the survey of small creatures, such as asari clam with a size of 3–5 cm [6].

To be accurate, all these systems must take into account both the propagation in water and sediment. However, the propagation of acoustic waves in sediments is generally much more complicated than in water because sediments are in general granular media composed of solid and fluid parts. The acoustic characteristics, such as the sound speed and the attenuation, can dramatically change with the ratio of the grain size to the wavelength [7]–[11]. Especially, as pointed out by Sessarego *et al.*, when the wavelength is smaller than the grain size, the effect of scattering becomes very strong and can considerably affect the signal structure [12]. This grain size dependence makes the understanding of signals more difficult and engineers have to rely on an empirical method for the design of the new subbottom devices, which results in an increase in the total cost of the sea surveys. As a consequence, the availability of a good prediction tool of the reflected signals from buried objects in granular media is critical to facilitate the design of these systems.

In this article, we propose to evaluate the performances of three different types of prediction tools for the simulation of backscattered signals by comparing them to experimental results obtained in a tank filled with water and several sets of calibrated glass beads having a wide range of ratios of the grain size to the wavelength.

The first type relies on the definition of a physical model. Many physical models with varying complexity have been developed for the modeling of acoustic wave propagation in marine sediments. For a review of the different models, which are

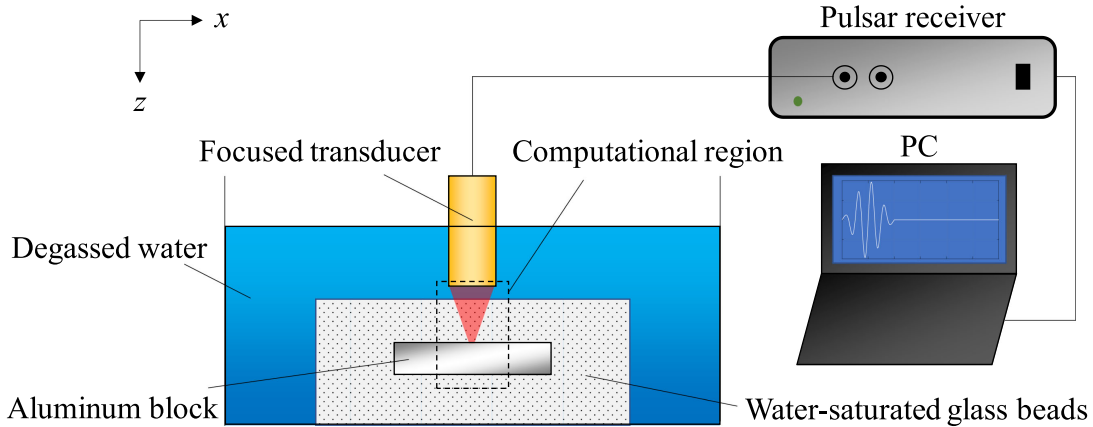


Fig. 1. Sketch of the experimental setup. In water, for a 1 MHz frequency, the 3-dB beamwidth of the probe is approximately 1.5 mm at the focal point. The amplitude of the input signal was  $100 V_{p-p}$ .

widely used in the underwater acoustics community, the reader is referred to the recent article from Ballard and Lee [13], which provides a state-of-art review of the research on the acoustics of marine sediments. Among the different models, two types are widely used: the Buckingham’s grain-shearing theory [14] and Biot’s theory [15], [16] with all its variants. In this article, we arbitrarily chose to use the Biot–Stoll model [17], [18]. This prediction tool will be referred to as BM hereafter.

Recently, in seismics, another type of model, called nonperiodic homogenization [19]–[21], was introduced to account for the presence of small heterogeneities (with respect to the minimum wavelength) in a homogeneous medium without having to mesh them explicitly. This method leads to the definition of an effective wave equation and an effective medium and has been successfully used. Since this approach may also hold for marine sediments, we propose to include it as a prediction tool and evaluate its performances. It will be the first time that such a model is used in the context of underwater acoustics and it will be referred to as HM hereafter.

Finally, with the advent of supercomputers, time-domain full-wave numerical methods are now able to produce accurate results even for highly heterogeneous models, such as marine sediments. With this approach, all beads will be explicitly considered and meshed. Such an approach is supposed to generate accurate numerical results although these results may be obtained at a very high computational cost. It will be the third type of prediction tool that we will consider and will be referred to as GM.

For all models, the generation of the numerical results will be based on a spectral element method (SEM) [22], [23].

## II. EXPERIMENTAL SETUP

In this section, we describe the experimental setup for imaging an aluminum block buried in a medium made of glass beads with controlled size. Signals backscattered from the aluminum block were recorded using the system illustrated in Fig. 1. The aluminum block had a length of 100 mm, a width of 20 mm, and a height of 20 mm. Signals were received by an acoustic

TABLE I  
EIGHT TYPES OF GLASS BEADS

Symbol	Grain diameter (mm)	$kd$	Grain size scale
GB1	0.038-0.053	0.19	Silt
GB2	0.075-0.090	0.35	Fine particle sand
GB3	0.125-0.150	0.58	Fine sand
GB4	0.180-0.250	0.90	Fine sand
GB5	0.250-0.355	1.35	Medium sand
GB6	0.355-0.500	1.79	Medium sand
GB7	0.500-0.710	2.53	Coarse sand
GB8	0.710-1.000	3.58	Coarse sand

focus probe of 30 mm in diameter having a focal distance of 32 mm (1-3 Piezocomposite, B1K25.4I PF38, Japan Probe Co., Ltd., Yokohama, Japan) and acting both as an emitter and a receiver. The probe generates square pulses in the time domain with a central frequency of 1 MHz. Eight types of glass beads (Fuji Manufacturing Co., Ltd., Tokyo, Japan) with different sizes were prepared (see Table I). In this table,  $kd$  represents the “wave number  $k$  (associated with the central frequency of the signal) times the mean grain diameter  $d$ .” An acrylic case was filled with water-saturated glass beads and set in a water tank. Then, the surrounding water and the water-saturated glass beads were boiled long enough to remove the possible remaining air bubbles. The water temperature was approximately 22 °C. The aluminum block was buried at a depth of about 28 mm below the glass bead surface to the surface of the block. A probe was then moved along the  $x$ -direction and signals were recorded on a laptop computer through a digital pulse receiver (JPR-300C, Japan Probe Co., Ltd., Yokohama, Japan) with a 10-MHz sampling rate. In the present study, for each glass bead sample, 70 signals were recorded along the  $x$ -direction with a 1-mm step.

## III. DIFFERENT PHYSICAL AND NUMERICAL MODELS

Wave propagation can be dramatically different with  $kd$  because of different physical phenomena. For example, absorption (e.g., due to grain resonances or pore fluid viscosity) is the dominant propagation loss mechanism in the low-frequency or

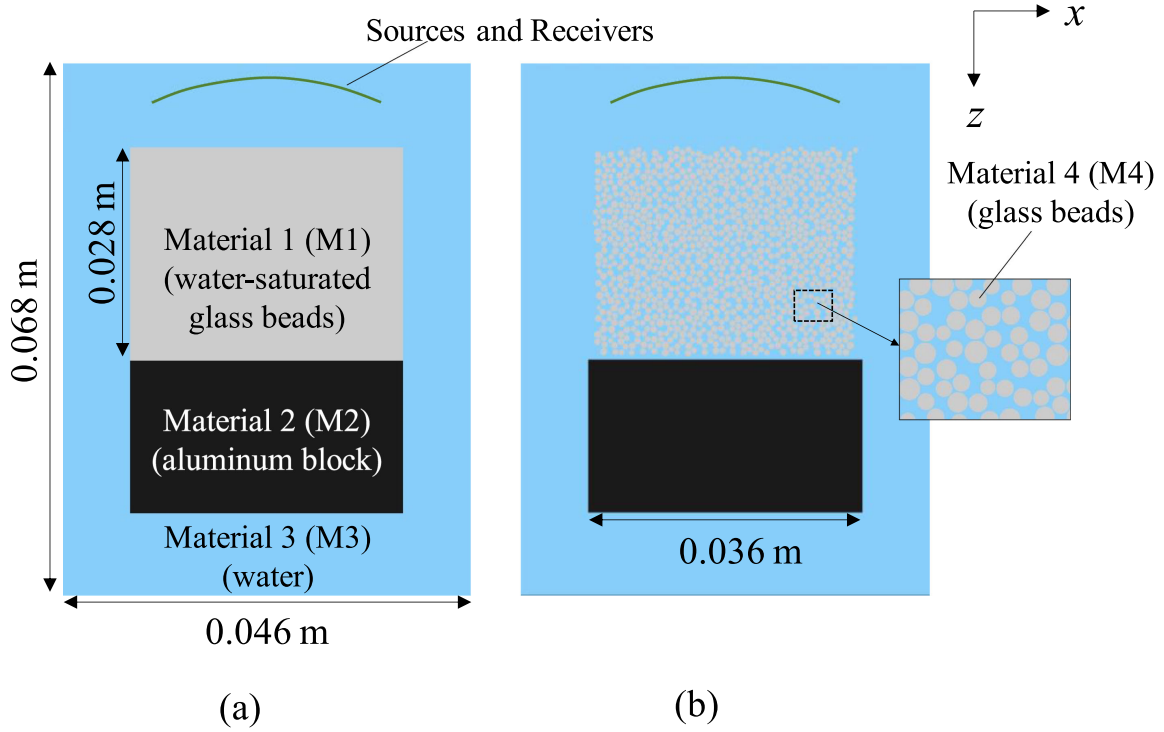


Fig. 2. Layout of the numerical models. Two different models (EM: Effective medium models and GM: Grain model) are considered in the numerical simulations. The size of the whole area is  $0.046 \times 0.068 \text{ m}^2$ . The 61 sources and receivers are shown as light green lines. In these configurations, the space between the sources/receivers is 0.5 mm in the  $x$ -direction. Four types of mediums are considered: M1, water with glass beads; M2, aluminum block; M3, water; and M4, glass beads. The values of the physical parameters are given in Table III.

small-diameter regime ( $kd \ll 1$ ) while scattering prevails in the high-frequency or large-diameter regime ( $kd \gg 1$ ) [6], [11], [12]. As a consequence, to cover all situations, different types of modeling have to be considered. As indicated in the introduction, we will consider, in a first step, two types of 2-D models, which provide effective physical properties of the granular medium. Then, in a second step, we perform numerical simulations that do not rely on effective properties by considering explicitly all grains and propagating acoustic waves in the complex medium as it stands. The two different types of models (BM and HM: effective medium models and GM: grain model) used to generate the numerical results are depicted in Fig. 2.

For all simulations, 61 equally spaced sources and receivers are set at the positions that simulate the size and curvature of the transducer, which is used in the experiments. A Gaussian pulse with 1 MHz center frequency is used as the source. The details of the models will be given in Sections III-B and III-C.

#### A. Solver

One of the most efficient ways of performing numerical simulations in the time domain for the solution of the full-wave equation is the spectral finite-element method. In this section, we recall the main characteristics of the spectral finite-element method and we focus only on some of its most important features. The SEM is based upon a high-order piecewise polynomial approximation of the weak formulation of the wave equation. It combines the accuracy of the pseudospectral method with the flexibility of the finite-element method. In this method, the

wavefield is represented in terms of high-degree Lagrange interpolants, and integrals are computed based upon Gauss–Lobatto–Legendre quadrature. This combination leads to a perfectly diagonal mass matrix, which in turn leads to a fully explicit time scheme that lends itself very well to numerical simulations on parallel computers.

In an elastic medium, the wave equation can be written in its strong equations form as

$$\rho \ddot{\mathbf{u}} - \nabla \cdot \boldsymbol{\sigma} = \mathbf{f} \quad (1)$$

$$\boldsymbol{\sigma} = \mathbf{c} : \boldsymbol{\varepsilon} = \lambda \text{tr}(\boldsymbol{\varepsilon}) \mathbf{I} + 2\mu \boldsymbol{\varepsilon} \quad (2)$$

$$\boldsymbol{\varepsilon} = \frac{1}{2} \left[ \nabla \mathbf{u} + (\nabla \mathbf{u})^T \right] \quad (3)$$

where  $\boldsymbol{\sigma}$  is the stress tensor,  $\mathbf{f}$  is an external force,  $\mathbf{c}$  is the elastic stiffness tensor,  $\boldsymbol{\varepsilon}$  is the strain tensor,  $\mathbf{u}$  is the displacement vector, and  $\rho$  is the density.  $\lambda$  and  $\mu$  are the two Lamé parameters,  $\text{tr}(\mathbf{A}) = \mathbf{A}_{ii}$  is the trace operator, and  $\mathbf{I}$  is the identity tensor.  $\nabla$  is the divergence operator,  $T$  is the transpose operator, and a dot over a symbol denotes time differentiation.

In fluid regions, the wave equation can be written in the following form:

$$\frac{1}{\kappa} \ddot{\chi} = \nabla \cdot \frac{1}{\rho} \nabla \chi \quad (4)$$

$$\mathbf{u} = \frac{1}{\rho} \nabla \chi \quad (5)$$

where  $\chi$  is a scalar potential and  $\kappa$  is the acoustic bulk modulus.



From a numerical point of view, it is more convenient to use this system because it allows for a numerical fluid–solid coupling, which is based on a noniterative scheme (see [44]).

It is particularly well suited to handling complex geometries and interface conditions. The use of a pseudospectral method also leads to the generation of coarser meshes. The typical element size that is required to generate an accurate mesh is of the order of  $\lambda$ ;  $\lambda$  being the smallest wavelength of waves traveling in the model. This comes from the fact that each spectral element, when using the SEM with a polynomial degree of  $N = 4$ , which is a typical value, contains a subgrid of  $(N + 1)^2 = 5 \times 5$  Gauss–Lobatto–Legendre discretization points and requires about five points per minimum wavelength of the problem under study. Very distorted mesh elements can be accurately handled. Complex models that include fluid, elastic, viscoelastic, anisotropic, or porous media can be modeled, making the SEM a method of choice for the numerical modeling of wave propagation through various types of media encountered in underwater acoustics. Results have been thoroughly validated with analytical codes and are used by many researchers in seismology all over the world. The reader is referred to [24, Ch. 4] for more details on the SEM and to [25] and [26] for a review of its capabilities for both forward and inverse modeling. Additionally, convolutional perfectly matched layers are used to remove spurious reflections from the boundaries of the computational domain [27]. Finally, the SEM is well suited for parallel implementations on supercomputers as well as on clusters of GPU cards by using the Message Passing Interface library and overlapping communications with calculations to hide their cost. This is an important feature for high-performance computing, which is absolutely necessary for the configurations we want to solve.

Several publications have already used its potential in underwater acoustics [28]–[30]. In this work, we will present a new application of the use of an SEM in this domain.

It must be noted that one of the main difficulties of the SEM is the mesh generation because it requires quadrangles in 2-D and hexahedra in 3-D. Depending on the geometry of the model, it can be very difficult or even impossible to generate a mesh. This is the case for the grain model where the distance between two grains can be very small. It also leads to a mesh, when it is possible to generate one, with very small elements (much smaller than the wavelength and thus unnecessary small). As a consequence, time-domain simulations will require very small time steps and the resulting numerical cost can be prohibitive. For the mesh generation, two meshing software were used: CUBIT/Trelis (developed by Sandia National Laboratories, Albuquerque, NM, USA) and Gmsh by Geuzaine and Remacle [31].

This solver will be used for the generation of the numerical results with the HM and GM models.

## B. Effective Medium Models (EM)

1) *Biot–Stoll Model (BM)*: In this first model, we consider that the space, which is occupied by the water-saturated glass beads (M1), is a homogeneous medium. The layout of the model is given in Fig. 2(a). As mentioned in the previous section, the physical parameters in water-saturated granular media, the

sound speed and attenuation, vary depending on the grain size. Such physical parameters can be evaluated using Biot–Stoll model [3], [7], [8], [11], [32]. The Biot–Stoll model is widely used and a useful tool to analyze the acoustic characteristics of water-saturated granular media. Kimura *et al.* summarized the characteristics of the Biot–Stoll model and reported some comparisons between analytical and experimental results [11], [32], [33]. Let us briefly recall the main characteristics of the Biot–Stoll model (more detailed information on the Biot–Stoll model can be found in [3], [7], [8], [17], [18], and [32]). The physical parameters of the equivalent model are derived using the equations of motion for the porous water-saturated granular media expressed in the following form:

$$\mu_b \nabla^2 \mathbf{u}_b + (H - \mu_b) \{ \nabla (\nabla \cdot \mathbf{u}_b) \} - C \{ \nabla (\nabla \cdot \mathbf{w}_b) \} = \rho_b \ddot{\mathbf{u}}_b - \rho_{bf} \ddot{\mathbf{w}}_b \quad (6)$$

$$C \{ \nabla (\nabla \cdot \mathbf{u}_b) \} - M \{ \nabla (\nabla \cdot \mathbf{w}_b) \} = \rho_{bf} \ddot{\mathbf{u}}_b - m \ddot{\mathbf{w}}_b - \frac{\eta F}{k_b} \dot{\mathbf{w}}_b \quad (7)$$

where

$$H = \frac{(K_r - K_b)^2}{D - K_b} + K_b + \frac{4}{3} \mu_b \quad (8)$$

$$C = \frac{K_r (K_r - K_b)}{D - K_b} \quad (9)$$

$$M = \frac{K_r^2}{D - K_b} \quad (10)$$

$$D = K_r^2 \left\{ \beta \frac{1}{K_f} + (1 - \beta) \frac{1}{K_r} \right\} \quad (11)$$

$$\mathbf{w}_b = \beta (\mathbf{u}_b - \mathbf{U}_b) \quad (12)$$

$$m = \alpha_b \frac{\rho_{bf}}{\beta}. \quad (13)$$

In these equations,  $\mu_b$  ( $\mu_b = \mu_{br} + j\mu_{bi}$ ) is the complex shear modulus of the frame,  $\mathbf{u}_b$  is the displacement vector of the frame,  $\mathbf{U}_b$  is the displacement vector of the pore fluid,  $\beta$  is the porosity,  $\rho_b = \beta \rho_{bf} + (1 - \beta) \rho_{br}$  is the density of water-saturated granular media,  $\rho_{bf}$  and  $\rho_{br}$  are the densities of the pore fluid and grain,  $m$  is the virtual mass, and  $\alpha_b$  is the structural factor when considering the nonuniformity of the pore fluid. The viscous resistance to fluid flow is given by the ratio  $\eta/k_b$  (where  $\eta$  is the fluid viscosity and  $k_b$  the permeability) and the viscous correction factor  $F$ . The quantities  $K_f$ ,  $K_r$ , and  $K_b$  ( $= K_{br} + jK_{bi}$ ) are the frame moduli of the pore fluid, the grain, and the frame, respectively. The frame bulk and shear moduli are given by

$$K_b = K_{br} \left( 1 + j \frac{\delta_l}{\pi} \right) \quad (14)$$

$$\mu_b = \mu_{br} \left( 1 + j \frac{\delta_s}{\pi} \right) \quad (15)$$

where  $\delta_l$  and  $\delta_s$  are the bulk and shear log decrements, respectively.

TABLE II  
PARAMETERS USED TO COMPUTE THE ACOUSTIC CHARACTERISTICS OF THE BIOT-STOLL MODEL

Parameter	Unit	GB1	GB2	GB3	GB4	GB5	GB6	GB7	GB8
<b>Grain</b>									
Diameter	mm	0.0455	0.0825	0.138	0.215	0.323	0.428	0.605	0.855
Density	kg/m <sup>3</sup>	2500	2500	2500	2500	2500	2500	2500	2500
Bulk modulus	Pa	3.60×10 <sup>10</sup>	3.60×10 <sup>10</sup>	3.60×10 <sup>10</sup>	3.60×10 <sup>10</sup>	3.60×10 <sup>10</sup>	3.60×10 <sup>10</sup>	3.60×10 <sup>10</sup>	3.60×10 <sup>10</sup>
<b>Fluid</b>									
Density	kg/m <sup>3</sup>	1000	1000	1000	1000	1000	1000	1000	1000
Bulk modulus	Pa	2.20×10 <sup>9</sup>	2.20×10 <sup>9</sup>	2.20×10 <sup>9</sup>	2.20×10 <sup>9</sup>	2.20×10 <sup>9</sup>	2.20×10 <sup>9</sup>	2.20×10 <sup>9</sup>	2.20×10 <sup>9</sup>
Viscosity	Pa·s	1.00×10 <sup>-3</sup>	1.00×10 <sup>-3</sup>	1.00×10 <sup>-3</sup>	1.00×10 <sup>-3</sup>	1.00×10 <sup>-3</sup>	1.00×10 <sup>-3</sup>	1.00×10 <sup>-3</sup>	1.00×10 <sup>-3</sup>
<b>Frame</b>									
Porosity	-	0.42	0.42	0.42	0.42	0.42	0.42	0.42	0.42
Permeability	m <sup>2</sup>	2.53×10 <sup>-12</sup>	8.33×10 <sup>-12</sup>	2.33×10 <sup>-11</sup>	5.66×10 <sup>-11</sup>	1.28×10 <sup>-10</sup>	2.24×10 <sup>-10</sup>	4.48×10 <sup>-10</sup>	8.94×10 <sup>-10</sup>
Pore size	m	1.10×10 <sup>-5</sup>	1.99×10 <sup>-5</sup>	3.33×10 <sup>-5</sup>	5.19×10 <sup>-5</sup>	7.80×10 <sup>-5</sup>	1.03×10 <sup>-4</sup>	1.46×10 <sup>-4</sup>	2.06×10 <sup>-4</sup>
Structure factor	$\alpha_b$	1.25	1.25	1.25	1.25	1.25	1.25	1.25	1.25
Bulk modulus (real part)	Pa	8.37×10 <sup>8</sup>	8.37×10 <sup>8</sup>	8.37×10 <sup>8</sup>	8.37×10 <sup>8</sup>	8.37×10 <sup>8</sup>	8.37×10 <sup>8</sup>	8.37×10 <sup>8</sup>	8.37×10 <sup>8</sup>
Bulk modulus (imaginary part)	Pa	4.00×10 <sup>7</sup>	4.00×10 <sup>7</sup>	4.00×10 <sup>7</sup>	4.00×10 <sup>7</sup>	4.00×10 <sup>7</sup>	4.00×10 <sup>7</sup>	4.00×10 <sup>7</sup>	4.00×10 <sup>7</sup>
Bulk logarithmic decrement	-	0.15	0.15	0.15	0.15	0.15	0.15	0.15	0.15
Shear modulus (real part)	Pa	3.86×10 <sup>6</sup>	3.86×10 <sup>6</sup>	3.86×10 <sup>6</sup>	3.86×10 <sup>6</sup>	3.86×10 <sup>6</sup>	3.86×10 <sup>6</sup>	3.86×10 <sup>6</sup>	3.86×10 <sup>6</sup>
Shear modulus (imaginary part)	Pa	1.84×10 <sup>5</sup>	1.84×10 <sup>5</sup>	1.84×10 <sup>5</sup>	1.84×10 <sup>5</sup>	1.84×10 <sup>5</sup>	1.84×10 <sup>5</sup>	1.84×10 <sup>5</sup>	1.84×10 <sup>5</sup>
Shear logarithmic decrement	-	0.15	0.15	0.15	0.15	0.15	0.15	0.15	0.15

In the harmonic regime, when a solution of the form of a longitudinal plane wave with a wave number  $k_l$  ( $k_l = k_{lr} + jk_{li}$ ) is sought, the following characteristic equation is obtained:

$$(C^2 - HM)k_l^4 + \left\{ \left( m - j \frac{\eta F}{k_b \omega} \right) H + \rho_b M - 2\rho_b f C \right\} \omega^2 k_l^2 + \left\{ \rho_b^2 - \rho_b \left( m - j \frac{\eta F}{k_b \omega} \right) \right\} \omega^4 = 0. \quad (16)$$

The roots of this characteristic equation yield the sound speeds of the longitudinal waves  $c_l = \omega/k_{lr}$  (m/s) and their attenuation coefficients  $\alpha_l = 8.69k_{li}$  (dB/m).

Similarly, the characteristic equation for a shear plane wave solution is

$$\left( m - j \frac{\eta F}{k_b \omega} \right) \mu_b k_s^2 + \left\{ \rho_b^2 - \rho_b \left( m - j \frac{\eta F}{k_b \omega} \right) \right\} \omega^2 = 0 \quad (17)$$

where  $k_s = k_{sr} + jk_{si}$ .

The root of this equation yields the sound speed of the shear wave  $c_s = \omega/k_{sr}$  (m/s) and its attenuation coefficient  $\alpha_s = 8.69k_{si}$  (dB/m).

The input parameters for the Biot–Stoll model are given in Table II. In this table, the physical parameters of the grains are taken from [34]. We measured the density of water-saturated glass beads accurately using a precise electrical scale and a measuring cup. This quantity was used for the porosity calculation. All other parameters were calculated using the equations given in [32]. In addition, the bulk and shear quality factors are required for the numerical simulations. The quality factors for the longitudinal wave  $Q_l$  and for the shear wave  $Q_s$  can be calculated using the following relations  $Q_l^{-1} = 0.037\lambda_l\alpha_l$  and  $Q_s^{-1} = 0.037\lambda_s\alpha_s$  [35]. They are related to the bulk and shear quality factors  $Q_\kappa$  and  $Q_\mu$  as follows [36], [37]:

$$Q_l^{-1} = \left( 1 - \frac{c_s^2}{c_l^2} \right) Q_\kappa^{-1} + \left( \frac{c_s^2}{c_l^2} \right) Q_\mu^{-1} \quad (18)$$

$$Q_s^{-1} = Q_\mu^{-1} \quad (19)$$

where  $\lambda_l$  and  $\lambda_s$  are the wavelength of longitudinal and shear waves. Finally, the physical parameters for the model are given in Table III.

2) *Nonperiodic Homogenization (HM)*: In recent years, the so-called “nonperiodic homogenization method” has emerged

TABLE III  
PHYSICAL PARAMETERS FOR THE SIMULATION

Symbol	$c_l$ (m s <sup>-1</sup> )	$c_s$ (m s <sup>-1</sup> )	$\rho$ (kg m <sup>-3</sup> )	$Q_\kappa$	$Q_\mu$	
M1	GB1	1775	50	1870	81	15
	GB2	1780	50	1870	114	17
	GB3	1782	50	1870	150	18
	GB4	1783	50	1870	185	19
	GB5	1784	50	1870	216	20
	GB6	1784	50	1870	235	20
	GB7	1785	50	1870	257	20
	GB8	1785	50	1870	275	20
M2	6260	3080	2700	-	-	
M3	1477	-	1000	-	-	
M4	5440	3515	2500	-	-	

as a general technique to compute the effective properties of a heterogeneous medium. For wave propagation numerical simulations, it can drastically reduce the computation cost due to small-scale features while preserving good accuracy [19]–[21]. This method basically uses the two-scale homogenization technique for the upscaling. The idea of the two-scale homogenization has emerged in the 1970s from research in mechanics [38] and was also applied to the study of elastic wave propagation [39]. However, it was still limited to the periodic case. In the last decade, Capdeville *et al.* successfully extended the periodic two-scale homogenization theory to the nonperiodic case for the elastic wave in 2-D and 3-D [19], [21] and for the acoustic case [20]. A comprehensive description of the nonperiodic homogenization technique can be found in [19]–[21]. In its current form, the nonperiodic homogenization can only handle heterogeneous media that are fully fluid, fully solid, or with small fluid inclusions in a solid matrix. As a consequence, the homogenization technique cannot consider the solid nature of grains and we will have to rely on a fluid approximation of the grain properties. Nevertheless, this approximation, which is necessary to be able to use the homogenization technique in its current state, may also give us interesting information about the influence of the shear properties of the grains thanks to the comparison with the results provided by the GM model, which can handle both fluid and solid grains. The main effect of this approximation can be found in [20]. Within the framework of the homogenization technique, the strong form of the equations governing the effective acoustic wavefield is expressed as follows:

$$\frac{1}{\kappa^*} \ddot{\chi}^* - \nabla \cdot \mathbf{u}^* = 0 \quad (20)$$

$$\mathbf{u}^* = \mathbf{L}^* \cdot \nabla \chi \quad (21)$$

where  $1/\kappa^*$  is the filtered version of  $1/\kappa$ ,  $\chi$  is the displacement scalar potential,  $\mathbf{u}^*$  is the effective displacement vector,  $\chi^*$  is the effective displacement scalar potential, and  $\mathbf{L}^*$  is a second-order tensor that may carry the effective density anisotropy. As a result, effective velocity and anisotropy maps representing the medium are obtained. These maps, which depend on the grain distribution, are then inserted into a wave equation solver able to handle anisotropy for the density [20]. An example of the

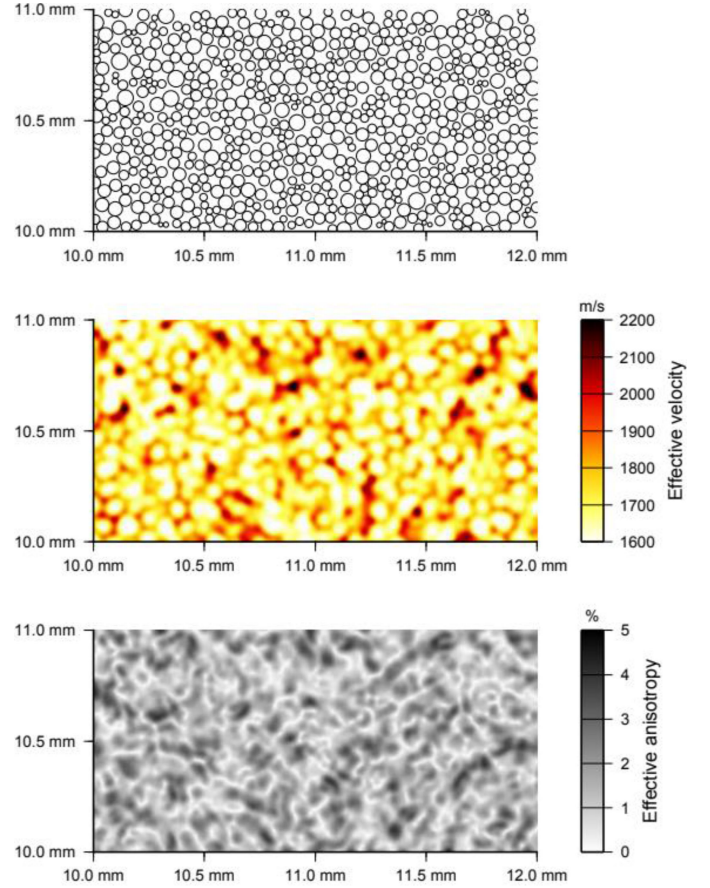


Fig. 3. Effective velocity and anisotropy maps generated by the nonperiodic homogenization approach. (Top: sample of the GB1 model with positions of the glass inclusion; Middle: effective velocity for the same sample; Bottom: inverse density anisotropy measured as, for each position, the matrix distance to the nearest isotropic inverse density matrix.)

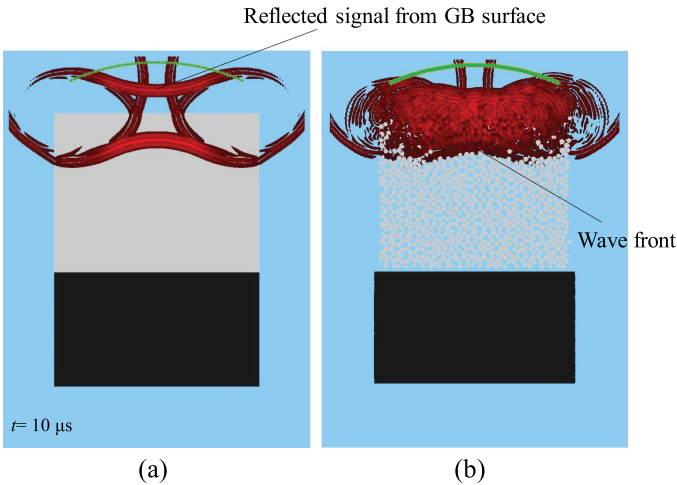
results provided by the nonperiodic homogenization approach together with the grain distribution is presented in Fig. 3. Once homogenized, the effective model can be used in the wave equation solver with a simple regular mesh [19]. In this study, as already mentioned in Section I, the numerical results will be obtained using an SEM.

### C. Grain Model (GM)

In this model, we chose to use a time-domain full-wave numerical model that does not rely on the approximation of a heterogeneous medium by an effective one. As a consequence, we have to consider each grain explicitly as shown in Fig. 2(b). This approach should provide the exact results but at the price of a computational cost, which can rapidly become prohibitive. The layout of the model is given in Fig. 2(b) and the physical parameters of the model are given in Table III. In this case, only media M2 (aluminum), M3 (water), and M4 (grain) are considered. The grains are disconnected, which means that there is always some water between two grains. The attenuation of the longitudinal and shear waves inside the grains is considered to be very small and thus neglected. The grain diameter, the number

TABLE IV  
GRAIN DISTRIBUTIONS

Symbol	Grain diameter (mm)	Number of grains	Porosity
GB1	0.045±0.010	327989	0.45
GB2	0.084±0.020	96399	0.44
GB3	0.140±0.033	35100	0.43
GB4	0.219±0.026	14762	0.44
GB5	0.345±0.037	6348	0.46
GB6	0.461±0.051	3363	0.46
GB7	0.620±0.062	1791	0.46
GB8	0.816±0.085	1005	0.45

Fig. 4. Snapshots at time  $t = 10 \mu\text{s}$ . Red color represents the norm of displacement.

of grains, and the porosity for the model are given in Table IV. The porosity was obtained by subtracting the sum of the areas of all grains to the area of the rectangle in which the grains are placed.

#### IV. RESULTS AND DISCUSSION

##### A. Comparison Between Waveforms Observed in Experiments and Simulations

First, we show the snapshots generated by two of the numerical methods namely the BM model and the GM model. The red color represents the norm of the displacement (magnitude of the displacement vector). These two snapshots (see Fig. 4) are obtained at the same time. In the GM simulation, we can see how the focusing of the emitted wave due to the concavity of the transducer is distorted by multiple scattering in the GM simulation. These snapshots are helpful for the understanding of wave propagation in the granular media.

Next, we show the typical waveforms that propagate in each sample for the eight kinds of water-saturated glass beads. The received waveforms obtained in the experiments are shown in Fig. 5. In this figure, multiple scattering is clearly seen and increases with grain size as well as the duration of the

reflected signal from the aluminum block. In Fig. 6, we present the numerical results using the BM model. In this case, the shape of the waveforms is similar with an amplitude slightly changing with grain size. Fig. 7 shows the results using the HM model, which uses the nonperiodic homogenization technique. As in Fig. 5, multiple scattering is clearly seen and increases with grain size. The duration of the signal reflected from the aluminum block also increases with grain size. Finally, we show the results using the GM model in Fig. 8 with similar results as in Fig. 7. For the GM model, the number of elements was very big for the grain size distribution GB6 and we were not able to get a mesh for the grain size distribution GB5 and smaller. All these waveforms obtained from numerical simulations are the result of the summation of the 61 signals received at the 61 receiver positions. The reflected waves coming from the surface of the glass bead medium and of the aluminum block are clearly detected in all data sets. They are found at approximately 12 and 45  $\mu\text{s}$ , respectively. To improve the dynamic range of the acquisition of the signals, the recorded emitted signal was saturated that prevents us from using it in the numerical simulations. We chose to use a Ricker wavelet as source time signal with a central frequency equal to the central frequency of the transducer. As a result, the emitted bandwidths in the experiments and in the numerical simulations are very different. However, the waveform changes with  $kd$  are clearly seen and some tendencies can still be found. As shown in Figs. 5, 7, and 8, multiple scattering is seen between the two reflected arrivals. It can also be seen that multiple scattering starts to appear for a value of  $kd$  around 1 and increases after. Multiple scattering is often considered as a “speckle noise” in images and affects their quality [6]. To quantify the variability of the signal amplitude due to multiple scattering, we define the root mean square (rms) value  $f_{\text{rms}}$  of the backscattered signal in the time interval  $[T_1, T_2]$  as

$$f_{\text{rms}} = \sqrt{\frac{1}{T_2 - T_1} \int_{T_1}^{T_2} [f(t)]^2 dt} \quad (22)$$

where  $f(t)$  is the backscattered signal and  $T_1$  and  $T_2$  are the beginning and end of the time interval in which we want to evaluate the level of multiple scattering. To quantify the variability with  $kd$ ,  $f_{\text{rms}}$  is normalized by its value for GB1 (for which multiple scattering is weak) for both the experimental and numerical results. Fig. 9 shows the variation with  $kd$  of normalized  $f_{\text{rms}}$  values calculated between 20  $\mu\text{s}$  ( $T_1$ ) and 40  $\mu\text{s}$  ( $T_2$ ) from experiments and the HM model. The normalized  $f_{\text{rms}}$  value increases with  $kd$  in both results. However, in the  $kd < 1$  regime, the normalized  $f_{\text{rms}}$  values given by the HM model are higher than the ones obtained from the experiment. In Fig. 5, it can be seen that the duration of the signal reflected from the top of the aluminum block increases with  $kd$ . This behavior is caused by the effect of velocity dispersion, especially, in  $kd > 1$  regime, and consistent with the results shown in previous studies [6], [11]. Since the bandwidths of the source signals used in the experiment and for the numerical simulation are different (the bandwidth for the numerical simulation is about two times wider), the signals are therefore different, however,



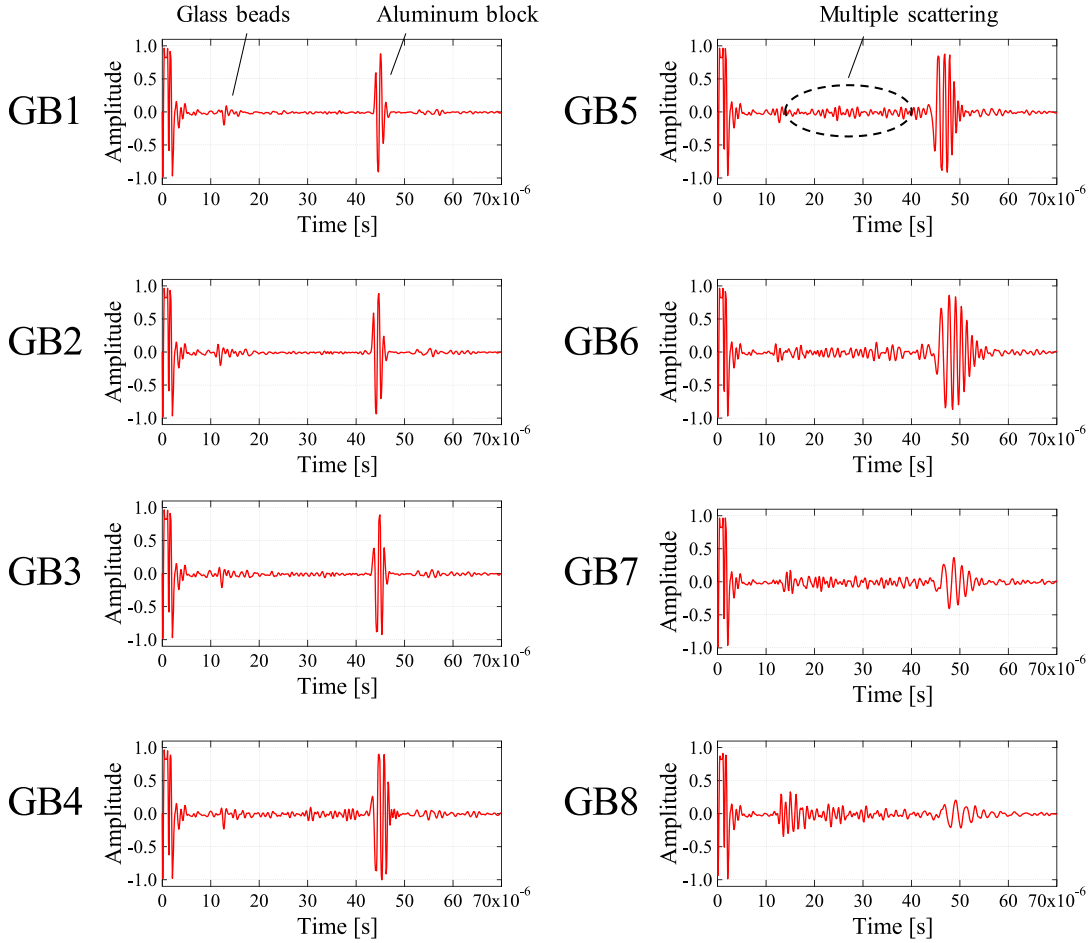


Fig. 5. Experimental signals obtained for different grain size distributions. The amplitude is normalized by the maximum value of the signal reflected from the aluminum block (in this case, the data are normalized with GB4 as a reference).

the evolution of their waveforms, with increasing value of  $kd$ , is similar.

Finally, to evaluate the impact of the approximation made in the HM model where the grains are considered as a fluid medium, we compare the signals obtained with the GM model and with the HM model using the same grain distribution size namely GB8. Since we can, with the GM model, either consider the grains as a fluid or an elastic medium, we use this possibility to evaluate the changes that this modification has on the time sequences. The results are shown in Fig. 10. It can be seen that when the grains are considered as a fluid medium, both models provide almost the same signal showing that the homogenization works very well in this configuration. Nevertheless, when the grains are considered as an elastic medium, the two time sequences are different. A small time shift of a few microseconds is observed on the position of the reflected signal from the top of the aluminum block.

### B. Effective Velocity and Effective Attenuation as a Function of $kd$

Another way of comparing the numerical results with the experimental ones is to evaluate from two signals two different quantities, which are characteristic of the propagation of the

acoustic wave through the granular medium. These two quantities, effective velocity and attenuation, are calculated from the envelope of the received signals. As indicated in Fig. 11, two distinct peaks can be detected from the envelope. The first peak corresponds to the reflection from the surface of the medium made of glass beads while the second peak corresponds to the reflection from the top surface of the aluminum block. The first quantity is a velocity, which can be obtained from the time difference between the first peak and the second peak using the thickness of the glass bead medium. The first peak is obtained using the signal between 10 and 40  $\mu\text{s}$ , whereas the second peak is obtained using the signal between 40 and 60  $\mu\text{s}$ . The second quantity is the ratio of the amplitude of these two peaks. It is related to the “apparent” attenuation due to the propagation through the granular medium. We denote these two quantities by effective velocity and effective attenuation.

Since it is difficult to determine exactly the arrival time of the first peak because of the roughness of the surface of the glass beads medium, especially in the high  $kd$  regime, we used the time of arrival of the first peak obtained with the grain distribution GB1 as a reference. The calculated effective velocity as a function of  $kd$  is shown in Fig. 12(a). The effective velocity obtained in the experiment is almost constant in the  $kd < 1$  regime (GB1–GB4) and dramatically decreases for  $kd > 1$

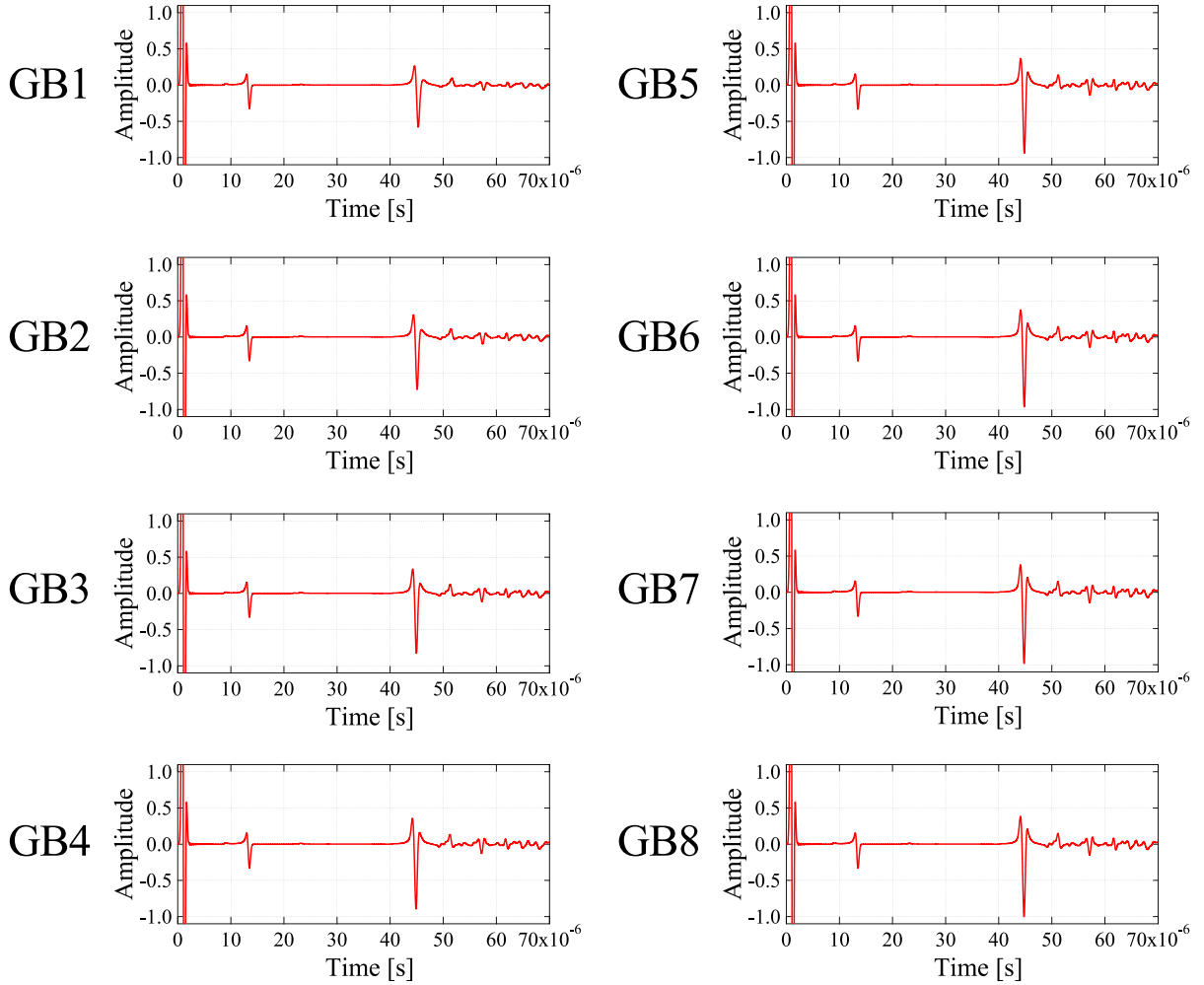


Fig. 6. Signals obtained with the BM model for different grain size distributions. The amplitude is normalized by the maximum value of the signal reflected from the aluminum block (in this case, the data are normalized with GB8 as a reference).

(GB5–GB8) regime. This decreasing is caused by the multiple scattering as shown by Schwartz and Plona [40] and consistent with a former study [6], [11]. The effective velocity obtained with the BM model is almost constant for the whole  $kd$  regime since the effect of multiple scattering is not taken into account in this model. The effective velocity obtained in the HM model, which uses homogenization, is almost constant for the  $kd < 1$  regime (GB1–GB4) and GB5, then decreases with  $kd$  in the higher  $kd$  region (GB6–GB8). The tendency of the effective velocity variations found in the experiments and the one given by the HM model is similar. However, the effective velocity we get from the experiments is higher than the one given by the HM model. In the  $kd$  regime where it was possible to get numerical results, the effective velocities given by the GM model are slower than the ones provided the HM model and closer to the results obtained from the experiment.

The variation with  $kd$  of the effective attenuation is shown in Fig. 12(b). In this figure, we chose to normalize the second peak by its value for the GB4 configuration. Therefore, for the value of  $kd$  corresponding to the GB4 configuration, the normalized effective attenuation will be equal to 0 dB. The effective

attenuation obtained in the experiment is almost constant for  $kd < 1$  regime (GB1–GB4) and dramatically decreased with  $kd$  for the  $kd > 1$  (GB5–GB8) regime. This high attenuation due to multiple scattering in the high  $kd$  regime was pointed out by Sessarego *et al.* [12]. The effective attenuation values obtained from the BM model are slightly increasing with  $kd$ . The tendency is different from the results provided by the experiments, especially in the high  $kd$  regime, since multiple scattering is not taken account in this model (only attenuation is considered). The effective attenuation values obtained with the HM model are decreasing with  $kd$ . The tendency is consistent with the results obtained from the experiments made in the high  $kd$  regime. However, it is different in the low  $kd$  regime because attenuation is not taken account in the HM model and attenuation due to multiple scattering becomes smaller in the low  $kd$  regime. It means that in this regime, intrinsic attenuation is stronger than attenuation due to multiple scattering. The effective attenuation values obtained with the GM model are almost the same as the ones obtained with the HM model. Here, since we were unable to get numerical results for GB4, the effective attenuation values were normalized with respect to the value obtained for GB4

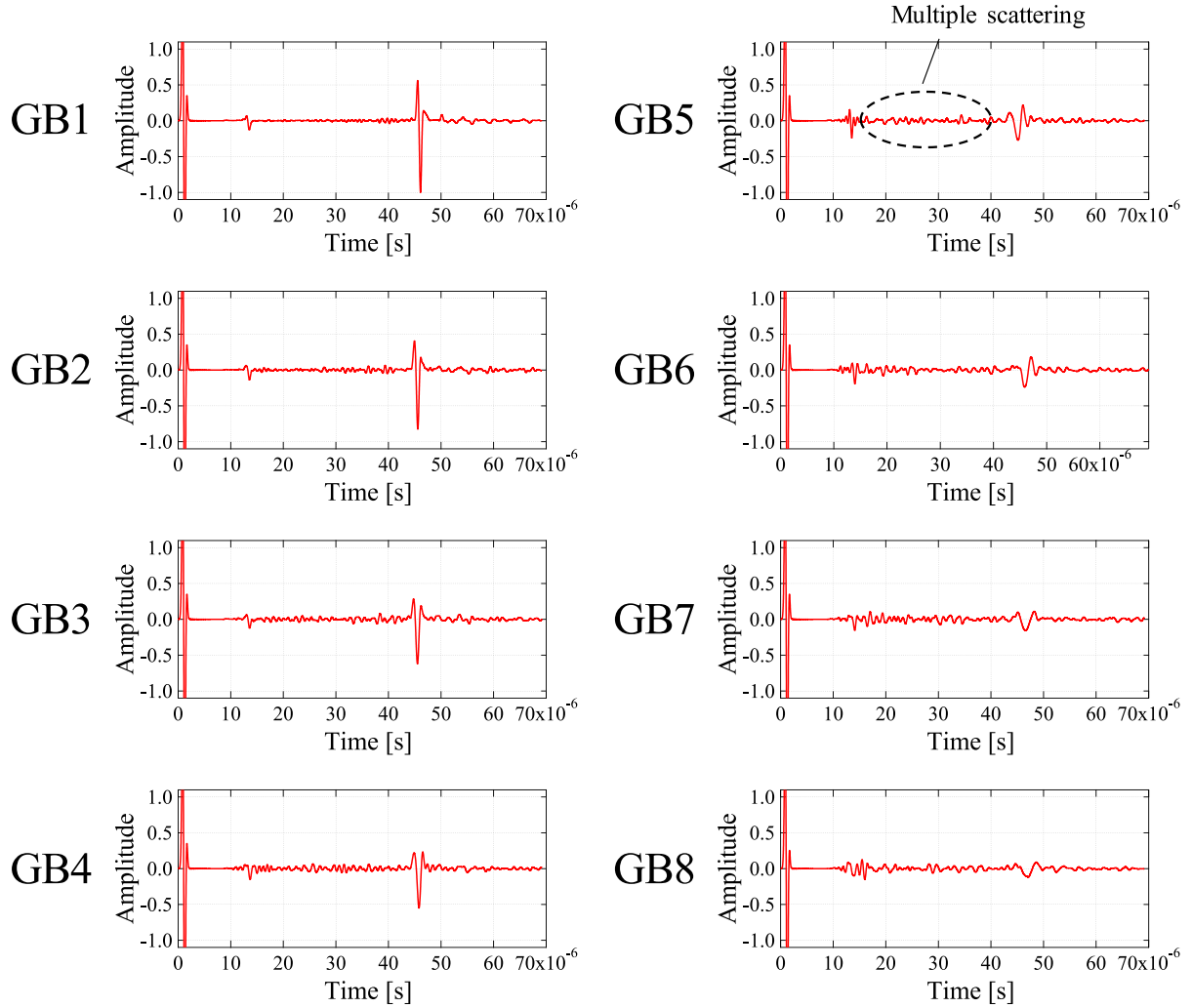


Fig. 7. Signals obtained with the HM model for different grain size distributions. The amplitude is normalized by the maximum value of the reflected signal from the aluminum block (in this case, the data are normalized with GB1 as a reference).

with the HM model. As shown in Fig. 12(b), the normalized effective attenuation for  $kd < 1$  with the HM model greatly differs from the experiment. As mentioned in the literature, the friction associated with grain motion and a change of the physical properties of the fluid in small interstitial spaces should have been considered [41], [42]. However, it is not possible to consider these effects in our grain models GM and HM. It may be at the origin of the discrepancy between the experimental and numerical results. From these results, we can see that the wave propagation characteristics in water-saturated granular media are dramatically changed around the transition region ( $kd = 1$ ). Therefore, we chose to change the numerical model depending on the  $kd$  regime. The effective velocity and effective attenuation are replotted in Fig. 13 using the two models. The result obtained with the BM model is used in low  $kd$  regime (GB1–GB4) and the HM model is used in high  $kd$  regime (GB5–GB8). In this way, we get a good agreement between the experiments and the numerical simulations.

### C. Comparison of the Computational Cost

For practical considerations, it is also important to compare the numerical cost of the different approaches. In Table V, for each grain size distribution, we give the number of elements of the mesh and the number of CPU hours required to perform the simulation. In this table, we do not take into account the time for the mesh generation, which can be nonnegligible. For the BM model, the number of elements and CPU hours were relatively high because of the low value of the velocity of shear wave which required to have small elements. For the GM model, the number of elements was very big for the grain size distribution GB6 mainly because of the very small distance between the grains, which was the main difficulty for the mesh generation and because we were not able to get a mesh for the grain size distribution GB5 and smaller. For the grain size distributions GB8 and GB7, we were able to get a mesh with the Trelis meshing software but Trelis failed to generate a mesh for GB6. Only the Gmsh meshing software was able to generate a mesh but at the price

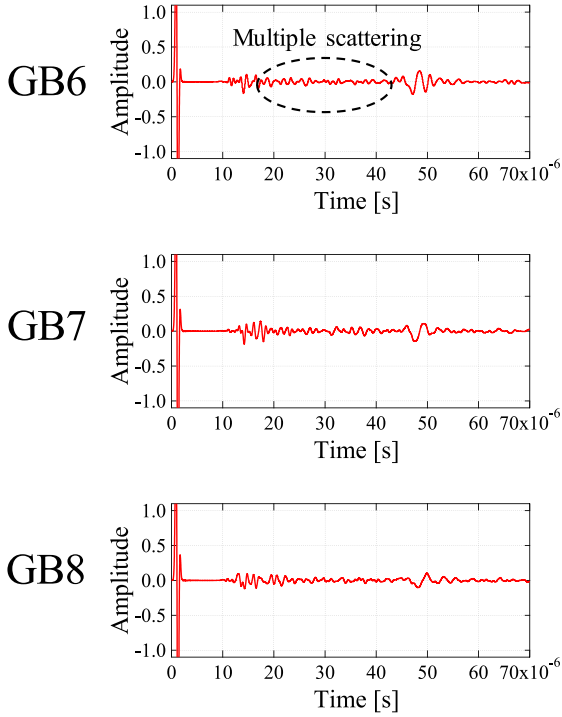


Fig. 8. Signal obtained with GM model for different grain size distributions. The amplitude is normalized by the maximum value of the signal reflected from the aluminum block (in this case, the data are normalized with GB4 from HM model as a reference).

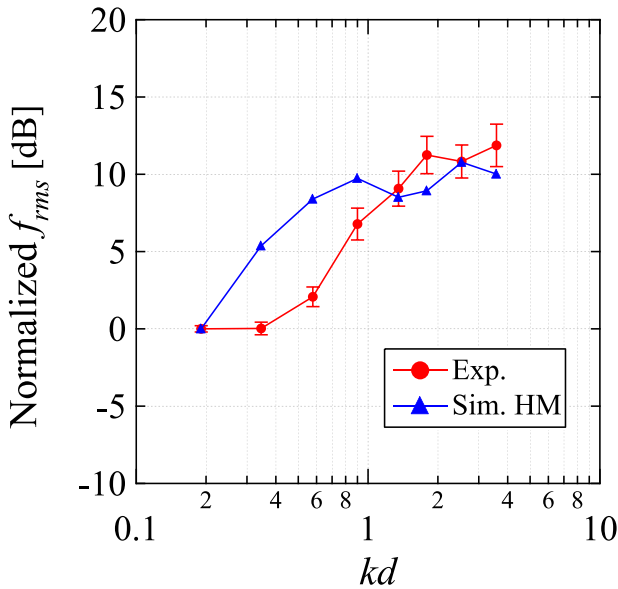


Fig. 9. Normalized  $f_{rms}$  value of backscattered signal amplitude obtained in the experiments (red circle and line) and the results obtained with the HM model (blue triangle and line) for different grain size distributions. The error bar shows the standard deviation calculated from 70 data sets.  $f_{rms}$  was calculated using the signal between 20 and 40  $\mu s$ .

of a very big number of elements. For GB7 and GB8, we were also able to generate a mesh with Gmsh but these meshes were much bigger than the ones obtained with Trelis, which were thus preferred. This is because there is a huge increase in the number of elements between GB7 and GB6. For the HM model, we

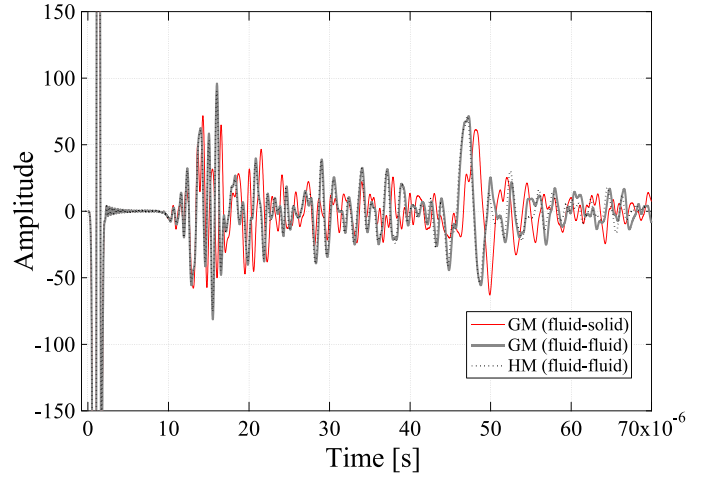


Fig. 10. Signals obtained for the grain size GB8. The two signals obtained with GM model are shown as full lines. The red line corresponds to a numerical simulation with fluid grains. The gray line corresponds to a numerical simulation with solid grains. The signal obtained with the HM model is the black dashed line.

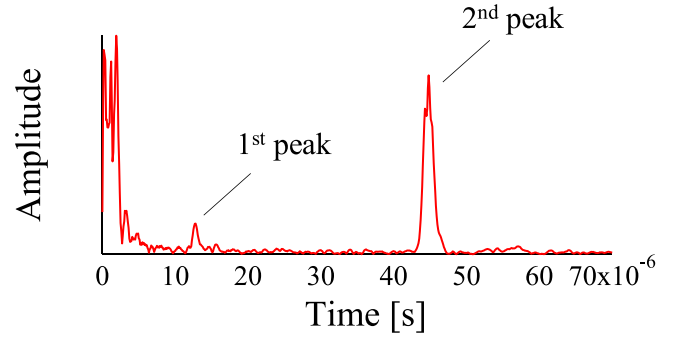


Fig. 11. Envelope of the experimental signal obtained with the grain distribution GB1.

were able to run the simulations for all grain size distributions, including the grain size distribution GB1 where the diameter of a grain was about 1/30th of the wavelength. Furthermore, the increase in the number of CPU hours required for performing the numerical simulation is moderate. This is due to the efficient parallelization and memory management of the SEM [43].

## V. CONCLUSION

In this study, backscattered signals from an object embedded in a water-saturated granular media were obtained experimentally and compared to the results provided by different numerical models. The predicted characteristic variations, as a function of grain size, of the waveforms, which propagate in a water-saturated granular media, were recovered in both experimental and numerical results.

Among the numerical models we considered, we found that the Biot–Stoll model provides good results in the low  $kd$  regime ( $kd < 1$ ), whereas the GM model, based on full-wave simulation, can provide good results in the high  $kd$  regime ( $kd > 1$ ). The main limitation of the GM model is related to obtain a reliable mesh. In addition, the third model that we considered, which uses the



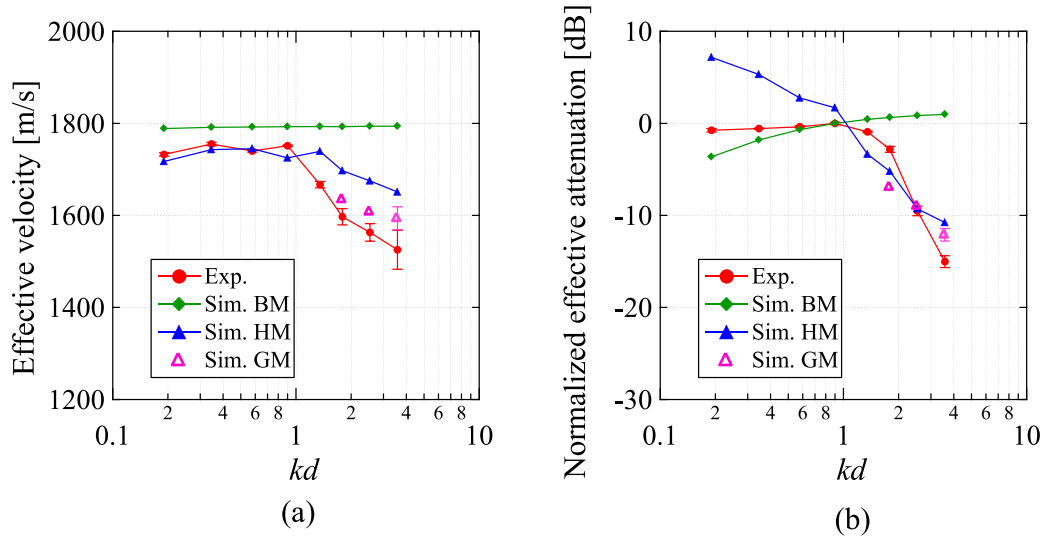


Fig. 12. (a) Effective velocity and (b) effective attenuation for different grain size distributions. The red color represents the experimental results. The error bar shows the standard deviation calculated from 70 data sets. The green color represents the numerical results obtained with BM model and the blue color represents the results obtained with the HM model. The pink triangles are the results obtained with the GM model. The error bar for the GB model at the highest  $kd$  (GB8) shows the standard deviation calculated using 11 data sets. Due to the computational cost, other error bars were not calculated.

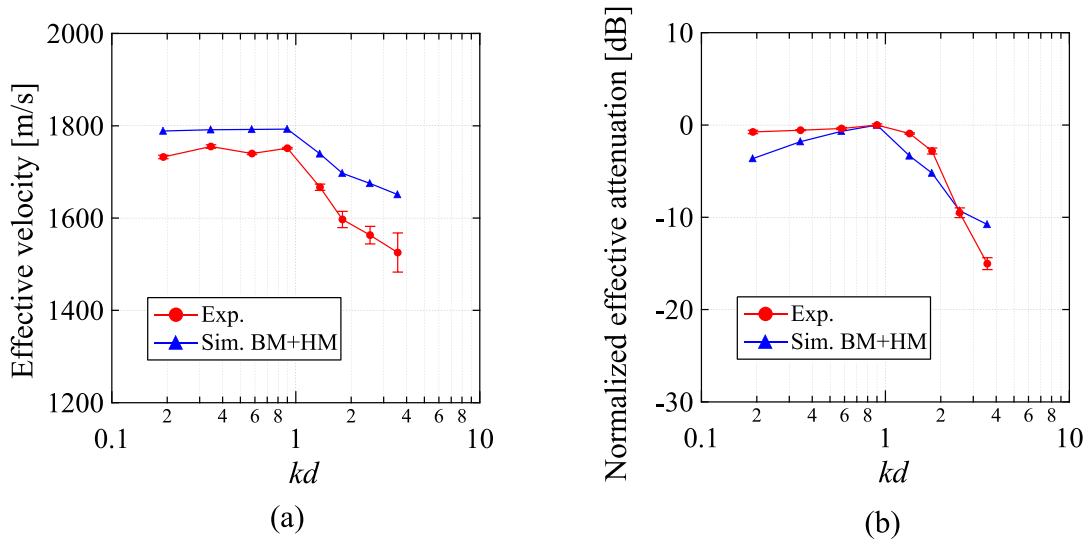


Fig. 13. (a) Effective velocity and (b) effective attenuation are shown. The experimental results correspond to the red line and the numerical results (blue line) are a mix of the results obtained with the BM model and the results obtained with the HM model. The results obtained with the BM model are used for the low  $kd$  regime (GB1–GB4) and the results obtained with the HM model are used for the high  $kd$  regime (GB5–GB8).

nonperiodic homogenization technique, happens to have a wide range of validity much wider than the other numerical models we used. In its current state, it is limited because it is not possible to consider solid inclusions in a fluid medium but the preliminary results we obtained are very encouraging. In particular, it is very efficient from the computational cost point of view, even for small grains.

Finally, the numerical models we used in the present study were 2-D. It is clear that, to be as close as possible to reality, 3-D simulations are required. Obviously, the GM model based on full-wave simulations cannot be used. The only choice will be to use the nonperiodic homogenization approach, but an extension of this approach, able to handle solid inclusions in a fluid medium, would probably be necessary.

TABLE V  
COMPUTATIONAL PERFORMANCE

Model	Number of mesh element	CPU·Hours			
		Homogenization	Solver (SEM)	Total	
BM	GB1	663,712	-	333	333
	GB2	663,712	-	323	323
	GB3	663,712	-	314	314
	GB4	663,712	-	305	305
	GB5	663,712	-	453	453
	GB6	663,712	-	442	442
	GB7	663,712	-	444	444
	GB8	663,712	-	361	361
GM	GB6	6,409,192	-	21,844	21,844
	GB7	456,949	-	60	60
	GB8	349,735	-	41	41
HM	GB1	14,805	36	21	57
	GB2	14,805	18	21	39
	GB3	14,805	17	21	38
	GB4	14,805	17	21	38
	GB5	14,805	5	21	26
	GB6	14,805	2	21	23
	GB7	14,805	1	21	22
	GB8	14,805	1	21	22

#### ACKNOWLEDGMENT

The authors would like to thank H. Suganuma, H. Muto, and R. Oshimi who were students in the Graduate School of Frontier Sciences, The University of Tokyo, and K. Ohira who works at Japan Probe Co. Ltd., for their assistances in conducting the experiments. The authors would also like to thank the Centre de Calcul Intensif de Pays de la Loire as some of the computations were performed with its resources. The authors would also like to dedicate this work to their colleague D. Komatitsch who passed away during its realization. The authors feel great honor for being able to work with him.

#### REFERENCES

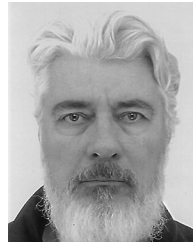
- [1] W. M. Tian, "Integrated method for the detection and location of underwater pipelines," *Appl. Acoust.*, vol. 69, no. 5, pp. 387–398, 2008.
- [2] R. M. Plets *et al.*, "The use of a high-resolution 3D Chirp sub-bottom profiler for the reconstruction of the shallow water archaeological site of the *Grace Dieu* (1439), River Hamble, UK," *J. Archaeological Sci.*, vol. 36, no. 2, pp. 408–418, 2009.
- [3] K. Mizuno, A. Asada, F. Katase, K. Nagahashi, T. Ura, and T. Haraguchi, "Development of the parametric sub-bottom profiler for autonomous underwater vehicles and the application of continuous wavelet transform for sediment layer detections," *J. Mar. Acoust. Soc. Jpn.*, vol. 43, no. 4, pp. 233–248, 2016.
- [4] K. Mizuno *et al.*, "Development and sea trial of the parametric sub-bottom profiler system for autonomous underwater vehicles-off Hatsushima Island," in *Proc. IEEE OCEANS Conf.*, Aberdeen, Scotland, 2017, pp. 1–4.
- [5] K. Mizuno *et al.*, "Automatic non-destructive three-dimensional acoustic coring system for in situ detection of aquatic plant root under the water bottom," *Case Stud. Nondestructive Test. Eval.*, vol. 5, pp. 1–8, 2016.
- [6] H. Suganuma, K. Mizuno, and A. Asada, "Application of wavelet shrinkage to acoustic imaging of buried asari clams using high-frequency ultrasound," *Jpn. J. Appl. Phys.*, vol. 57, no. 7S1, 2018, Art. no. 07LG08.
- [7] R. D. Stoll, *Sediment Acoustics*. Berlin, Germany: Springer-Verlag, 1989.
- [8] R. D. Stoll, "Velocity dispersion in water-saturated granular sediment," *J. Acoust. Soc. Amer.*, vol. 111, no. 2, pp. 785–793, 2002.
- [9] K. L. Williams, D. R. Jackson, E. I. Thorsos, D. Tang, and S. G. Schock, "Comparison of sound speed and attenuation measured in a sandy sediment to predictions based on the Biot theory of porous media," *IEEE J. Ocean. Eng.*, vol. 27, no. 3, pp. 413–428, Jul. 2002.
- [10] N. P. Chotiros, A. M. Mautner, A. Lovik, A. Kristensen, and O. Bergem, "Acoustic penetration of a silty sand sediment in the 1-10-kHz band," *IEEE J. Ocean. Eng.*, vol. 22, no. 4, pp. 604–615, Oct. 1997.
- [11] M. Kimura, "Velocity dispersion and attenuation in granular marine sediments: Comparison of measurements with predictions using acoustic models," *J. Acoust. Soc. Amer.*, vol. 129, no. 6, pp. 3544–3561, 2011.
- [12] J. P. Sessarego, A. N. Ivakin, and D. Ferrand, "Frequency dependence of phase speed, group speed, and attenuation in water-saturated sand: Laboratory experiments," *IEEE J. Ocean. Eng.*, vol. 33, no. 4, pp. 359–366, Oct. 2008.
- [13] M. S. Ballard and K. M. Lee, "The acoustics of marine sediments," *Acoust. Today*, vol. 13, no. 3, pp. 11–18, 2017.
- [14] M. J. Buckingham, "Wave propagation, stress relaxation, and grain-to-grain shearing in saturated, unconsolidated marine sediments," *J. Acoust. Soc. Amer.*, vol. 108, no. 6, pp. 2796–2815, 2000.
- [15] M. A. Biot, "Theory of elastic waves in a fluid-saturated porous solid. I. Low frequency range," *J. Acoust. Soc. Amer.*, vol. 28, pp. 168–178, 1956.
- [16] M. A. Biot, "Theory of propagation of elastic waves in a fluid-saturated porous solid. II. Higher frequency range," *J. Acoust. Soc. Amer.*, vol. 28, no. 2, pp. 179–191, 1956.
- [17] R. D. Stoll and G. M. Bryan, "Wave attenuation in saturated sediments," *J. Acoust. Soc. Amer.*, vol. 47, no. 5B, pp. 1440–1447, 1970.
- [18] R. D. Stoll, "Acoustic waves in ocean sediments," *Geophysics*, vol. 42, no. 4, pp. 715–725, 1977.
- [19] Y. Capdeville, L. Guillot, and J. J. Marigo, "2-D non-periodic homogenization to upscale elastic media for P–SV waves," *Geophys. J. Int.*, vol. 182, no. 2, pp. 903–922, 2010.
- [20] P. Cance and Y. Capdeville, "Validity of the acoustic approximation for elastic waves in heterogeneous media," *Geophysics*, vol. 80, no. 4, pp. T161–T173, 2015.
- [21] P. Cupillard and Y. Capdeville, "Non-periodic homogenization of 3-D elastic media for the seismic wave equation," *Geophys. J. Int.*, vol. 213, no. 2, pp. 983–1001, 2018.
- [22] D. Komatitsch and J. P. Vilotte, "The spectral element method: An efficient tool to simulate the seismic response of 2D and 3D geological structures," *Bull. Seismol. Soc. Amer.*, vol. 88, no. 2, pp. 368–392, 1998.

- [23] D. Komatitsch and J. Tromp, "Introduction to the spectral element method for three-dimensional seismic wave propagation," *Geophys. J. Int.*, vol. 139, no. 3, pp. 806–822, 1999.
- [24] A. Fichtner, *Full Seismic Waveform Modelling and Inversion*. Berlin, Germany: Springer-Verlag, 2010.
- [25] D. Komatitsch and J. P. Vilotte, "The spectral element method: An efficient tool to simulate the seismic response of 2D and 3D geological structures," *Bull. Seismol. Soc. Amer.*, vol. 88, no. 2, pp. 368–392, 1998.
- [26] D. Peter *et al.*, "Forward and adjoint simulations of seismic wave propagation on fully unstructured hexahedral meshes," *Geophys. J. Int.*, vol. 186, no. 2, pp. 721–739, 2011.
- [27] D. Komatitsch and R. Martin, "An unsplit convolutional perfectly matched layer improved at grazing incidence for the seismic wave equation," *Geophysics*, vol. 72, no. 5, pp. SM155–SM167, 2007.
- [28] P. Cristini and D. Komatitsch, "Some illustrative examples of the use of a spectral-element method in ocean acoustics," *J. Acoust. Soc. Amer.*, vol. 131, no. 3, pp. EL229–EL235, 2012.
- [29] Z. Xie, R. Matzen, P. Cristini, D. Komatitsch, and R. Martin, "A perfectly matched layer for fluid-solid problems: Application to ocean-acoustics simulations with solid ocean bottoms," *J. Acoust. Soc. Amer.*, vol. 140, pp. 165–175, 2016.
- [30] A. Bottero, P. Cristini, D. Komatitsch, and M. Asch, "An axisymmetric time-domain spectral-element method for full-wave simulations: Application to ocean acoustics," *J. Acoust. Soc. Amer.*, vol. 140, no. 5, pp. 3520–3530, 2016.
- [31] C. Geuzaine and J. F. Remacle, "Gmsh: A 3-D finite element mesh generator with built-in pre- and post-processing facilities," *Int. J. Numer. Methods Eng.*, vol. 79, no. 11, pp. 1309–1331, 2009.
- [32] M. Kimura, "Study on the Biot–Stoll model for porous marine sediments," *Acoust. Sci. Technol.*, vol. 28, no. 4, pp. 230–243, 2007.
- [33] M. Kimura, "Shear wave speed dispersion and attenuation in granular marine sediments," *J. Acoust. Soc. Amer.*, vol. 134, no. 1, pp. 144–155, 2013.
- [34] M. Kimura, "Experimental investigation of temperature dependence of longitudinal wave velocity and attenuation in marine sediment model using the Biot–Stoll model," (in Japanese) *J. Mar. Acoust. Soc. Jpn.*, vol. 30, no. 3, pp. 181–188, 2003.
- [35] M. B. Porter, "The KRAKEN normal mode program," Nav. Res. Lab., Washington, DC, USA, Tech. Rep. NRL/MR/5120-92-6920, 1992.
- [36] F. A. Dahlen and J. Tromp, *Theoretical Global Seismology*. Princeton, NJ, USA: Princeton Univ. Press, 1998.
- [37] J. M. Carcione, D. Kosloff, and R. Kosloff, "Wave propagation simulation in a linear viscoelastic medium," *Geophys. J. Int.*, vol. 95, no. 3, pp. 597–611, 1988.
- [38] A. Bensoussan, J. L. Lions, and G. Papanicolaou, *Asymptotic Analysis for Periodic Structures*, vol. 374. Providence, RI, USA: Amer. Math. Soc., 2011.
- [39] J. Fish and W. Chen, "Space–time multiscale model for wave propagation in heterogeneous media," *Comput. Methods Appl. Mech. Eng.*, vol. 193, no. 45–47, pp. 4837–4856, 2004.
- [40] L. Schwartz and T. J. Plona, "Ultrasonic propagation in close-packed disordered suspensions," *J. Appl. Phys.*, vol. 55, no. 11, pp. 3971–3977, 1984.
- [41] N. P. Chotiros and M. Isakson, "A broadband model of sandy ocean sediments: Biot–Stoll with contact squirt flow and shear drag," *J. Acoust. Soc. Amer.*, vol. 116, no. 4, pp. 2011–2022, 2004.
- [42] N. P. Chotiros, *Acoustics of the Seabed as a Poroelastic Medium*. Cham, Switzerland: Springer, 2017, pp. 1–99.
- [43] S. Tsuboi, K. Ando, T. Miyoshi, D. Peter, D. Komatitsch, and J. Tromp, "A 1.8 trillion degrees-of-freedom, 1.24 petaflops global seismic wave simulation on the K computer," *Int. J. High Perform. Comput. Appl.*, vol. 30, no. 4, pp. 411–422, 2016. [Online]. Available: <https://doi.org/10.1177/1094342016632596>
- [44] E. Chaljub and B. Valette, "Spectral element modelling of three-dimensional wave propagation in a self-gravitating earth with an arbitrarily stratified outer core," *Geophys. J. Int.*, vol. 158, pp. 131–141, 2004.



**Katsunori Mizuno** received the Bachelor of Engineering, Master of Engineering, and Doctor of Engineering degrees from Doshisha University, Kyoto, Japan, in 2006, 2008, and 2012, respectively.

From 2008 to 2012, he was an Engineer with the Image Sensor Business Unit, Panasonic Corporation. From 2012 to 2017, he was a Projective Research Associate with the Institute of Industrial Science, The University of Tokyo, Tokyo, Japan, where he joined several national projects and developed various types of sonar systems. In 2017, he joined the Graduate School of Frontier Sciences, The University of Tokyo as an Assistant Professor. He was a Guest Researcher with the Laboratory of Mechanics and Acoustics, Centre National de La Recherche Scientifique, France, from 2018 to 2019, and a Guest Researcher with the National Oceanography Centre, University of Southampton, Southampton, U.K., in 2019. He is currently involved in the development of a new underwater sensing system for the monitoring of underwater environment and its applications.



**Paul Cristini** (Member, IEEE) graduated from the Ecole Nationale Supérieure de Physique de Marseille, Marseille, France, in 1986, and received the M.S. degree in underwater acoustics from DEA d'Acoustique, Marseille, France, in 1988 and the Ph.D. degree in underwater acoustics from the Université d'Aix-Marseille II, Marseille, France, in 1991.

He was a Researcher with the Centre National de la Recherche Scientifique. From 1991 to 2000, he was with the Laboratoire de Mécanique et d'Acoustique (LMA), Marseille, France, and from 2000 to 2008, with the Modélisation et Imagerie en Géophysique, Université de Pau, Pau, France. Since 2008, he has been with LMA, working on numerical modeling of wave propagation in underwater acoustics for various applications with emphasis on the use of high-performance computing.

Dr. Cristini is a member of the Acoustical Society of America and the French Acoustical Society.



**Dimitri Komatitsch** received the Ph.D. degree in spectral and spectral-element methods for 2-D and 3-D elastodynamics equations in heterogeneous media from the Institut de Physique du Globe de Paris, Paris, France, in 1997, and the Postdoctoral degree in advanced numerical modeling in geophysics from Harvard University, Cambridge, MA, USA, in 1999.

From 2000 to 2003, he was a Senior Research Fellow with the California Institute of Technology, Pasadena, CA, USA. In 2003, he became a Full Professor with the University of Pau, Pau, France, and in 2011, he became a Research Director with Centre National de la Recherche Scientifique, Marseille, France. He was a former member of the Institut Universitaire de France. His research interests include acoustic, ultrasonic and seismic wave propagation, imaging and inversion, as well as high-performance numerical simulations, and full waveform inversion.

Dr. Komatitsch was an Associate Editor for the international journals *Geophysics* and *Heliyon*. He was the recipient of the Gordon Bell International Award as well as the BULL Joseph Fourier Award for high-performance computing. He was also the recipient of an award from the Del Duca Foundation of the French Academy of Sciences. He passed away on January 21, 2019.



**Yann Capdeville** received the Ph.D. degree in coupling of the spectral element and normal mode methods for seismic wave propagation at the global scale from the Université de Paris 7, Paris, France, in 2000.

From 2000 to 2003, he was with the UC Berkeley Seismological Laboratory, Berkeley, CA, USA, as a Miller Fellow Postdoc. From 2003 to 2010, he was with the Centre National de la Recherche Scientifique, at the Institut de Physique du Globe de Paris as a Junior Researcher. Since 2010, he has been with the Centre National de la Recherche Scientifique in the Laboratoire de Planétologie et de Géodynamique de l'université de Nantes, first as a Junior Researcher and then as a Senior Researcher. His research interests include wave propagation and seismic inverse problems in complex media.